PAPER

Synthesis and interfacial engineering of nitride– halide electrolytes in all-solid-state Li batteries†

Yuxi Deng,[a] Ziteng Liang,[a] Ruqin Ma,[a] Yingao Zhou,[a] Yu Su,[a] Haoyue Zhong,[a] Weilin Huang,[a] Siyuan Pan,[a] Yu Luo,[a] Zihao Qin,[a] Yanxin Chen,[a] Zhengliang Gong [ID] [b] and Yong Yang [ID] *[a]

Halide solid-state electrolytes have attracted significant interest due to their high room-temperature ionic conductivity and electrochemical oxidation stability. However, their reliance on rare-earth metal-centered frameworks (*e.g.*, Y, In, Sc, and La) results in high costs and susceptibility to reduction. As a cost-effective alternative, Li_2ZrCl_6 leverages the earth abundance of zirconium but suffers from relatively low ionic conductivity ($\sim 10^{-4}$ S cm^{-1}), limiting its performance. Here, we report the synthesis of an amorphous nitride– halide electrolyte, $Li_{2+2x}ZrCl_{6-x}N_x$ (LZC-Nx, $0 \leq x \leq 0.25$), which simultaneously enhances ionic transport and anodic interfacial stability. The optimized LZC-N0.15 exhibits a twofold increase in room-temperature ionic conductivity (1.5 mS cm^{-1}) compared to LZC. The *in situ* formed N-rich interfacial layer enables a Li/ Li symmetric battery to achieve stable cycling for over 3000 hours with a critical current density of 2.8 mA cm^{-2}. Notably, LZC-N0.15 maintains compatibility with high-voltage cathodes while improving anodic stability. The all-solid-state battery employing an LZC-N0.15 electrolyte and a $LiCoO_2$ cathode delivers a high discharge capacity of 218.4 mAh g^{-1} at 4.62 V.

Broader context

All-solid-state lithium batteries are widely regarded as the most promising next-generation energy storage technology due to their exceptional combination of high energy density and intrinsic safety. Among various solid electrolytes, halide solid electrolytes have emerged as a research hotspot owing to their excellent high-voltage stability and superior room-temperature lithium-ion conductivity. However, the inherent high reduction potential of halide electrolytes remains a critical bottleneck, limiting their practical performance. This work focuses on cost-effective Li_2ZrCl_6, innovatively synthesizing a nitride–halide electrolyte $Li_{2+2x}ZrCl_{6-x}N_x$ ($0 \leq x \leq 0.25$) by high-energy ball milling. In contrast to conventional fluorine-doping strategies that often compromise ionic conductivity, our nitrogen-doping approach simultaneously enhances ionic conductivity and anode interface stability. Through comprehensive characterization studies, we systematically elucidate the structural evolution and ion-transport enhancement mechanisms. Notably, an *in situ* formed gradient interfacial layer (Li_3N- enriched on the lithium metal side and LiCl-aggregated on the electrolyte side) enables stable cycling of Li symmetric batteries, high critical current density, and breakthrough rate capability and discharge specific capacity in halide-based all-solid-state lithium batteries.

Introduction

In pursuit of battery technologies with higher energy density and enhanced safety, all-solid-state batteries (ASSBs) have emerged as

[a]*State Key Laboratory for Physical Chemistry of Solid Surface, Department of Chemistry, College of Chemistry and Chemical Engineering, Xiamen University, Xiamen, 361005, China. E-mail: dyx240827@163.com, 2569958121@qq.com, mm630532665@163.com, 1208954946@qq.com, suyuxmu@126.com, 13585578694@163.com, 15606390950@163.com, sypann@outlook.com, l1194025672@163.com, qinzihaobsh@163.com, xyanxinc@163.com, yyang@xmu.edu.cn*
[b]*College of Energy, Xiamen University, Xiamen, 361102, China. E-mail: zlgong@xmu.edu.cn*
†Electronic supplementary information (ESI) available. See DOI: https://doi.org/ 10.1039/d5eb00116a

a transformative strategy, enabling the safe implementation of lithium metal anodes.[1] However, to date, no single class of solid-state electrolytes (SSEs) simultaneously fulfills all desired physico-chemical properties. Sulfide SSEs, while exhibiting exceptional ionic conductivity and favorable mechanical properties, suffer from inevitable interfacial reactions with cathode materials.[2] Oxide SSEs demonstrate superior chemical stability but require high-temperature sintering to mitigate severe solid–solid contact issues.[3] Polymer SSEs with a flexible backbone exhibit inadequate room-temperature ionic conductivity, often necessitating elevated operating temperatures or liquid electrolyte additives and inherent oxidative instability under high voltages.[4] Before 2018, halide SSEs attracted limited attention due to their suboptimal room-temperature ionic conductivity. Asano *et al.*[5] synthesized yttrium-based halides Li_3YCl_6 and Li_3YBr_6, achieving break-

through ionic conductivities of 0.51 mS cm^{-1} and 0.72 mS cm^{-1} at 25 °C, respectively. Since then, halide electrolytes have experienced rapid development. Despite challenges including high reduction potentials and costs, their superior ionic conductivity, oxidation resistance, and deformability position halide SSEs as promising electrolyte systems for next-generation ASSBs.[6]

Lithium metal anodes, with their ultra-high theoretical capacity of 3861 mAh g^{-1} and an extremely low reduction potential of −3.04 V *versus* the standard hydrogen electrode, are widely regarded as the "Holy Grail" anode material for high-energy batteries.[7] The instability between halide SSEs and lithium metal predominantly originates from transition metal elements within the halide structure. Fu *et al.* systematically investigated interfacial interactions between lithium anodes and two representative Li$_3$YX$_6$ (X = Cl and Br) electrolytes through analysis of reaction product molar ratios and phase characteristics.[8] Upon contact, electrolytes form non-self-limiting interfacial phases that persistently react, undergoing reduction to LiX and Y. This process generates mixed ion/electron conductors, enabling concurrent Li$^+$ and e$^-$ transport through the decomposed layer to propagate further electrolyte degradation. Riegger *et al.* corroborated this reaction mechanism through studies on Li$_3$MCl$_6$ (M = In and Y) systems, deriving an identical reaction eqn (1).[9] For Li$_3$InCl$_6$-based lithium symmetric batteries, time-dependent impedance spectroscopy revealed progressive interfacial resistance growth, indicative of persistent interphase development at the SEs/Li interface.

$$\text{Li}_3\text{MCl}_6 + 3\text{Li} \rightarrow 6\text{LiCl} + \text{M}^0 \quad (\text{M} = \text{In and Y}) \quad (1)$$

Common modification strategies to enhance the anode stability of halide-based ASSBs include: (1) bilayer electrolyte architectures using sulfide SSEs as separators between the anode and halide SSEs, though introducing new interfacial challenges;[10] (2) fluorine doping to induce *in situ* interfacial layer formation during cycling, often at the expense of ionic conductivity;[11] and (3) artificial interfacial engineering using materials like Li$_3$N as protective coatings, though complicating fabrication processes.[12] These approaches reflect the trade-offs between interfacial stability, ionic transport properties, and manufacturing scalability in halide electrolyte systems.

In contrast to conventional chloride SEs (M = Y, In, Sc, and La), zirconium-based Li$_2$ZrCl$_6$ (LZC) emerges as a cost-competitive alternative, leveraging zirconium's crustal abundance, albeit compromised by suboptimal ionic conductivity (10^{-4} S cm^{-1}) and electrochemical stability.[13] This work pioneers an innovative nitrogen-doping strategy to enhance LZC's comprehensive performance. Nitride–halide SEs were successfully synthesized *via* high-energy ball milling, achieving a 1.5 mS cm^{-1} room-temperature ionic conductivity at x = 0.15, nearly twice that of pristine LZC, alongside reduced electronic conductivity, improved densification, and reinforced stability. Multimodal characterization (XRD, Raman, XPS, ^{7}Li ssNMR, and XAS) revealed that the conductivity enhancement stems from synergistic effects of lattice volume expansion, increased lithium-ion stoichiometry, and the formation of amorphous phases. Furthermore, assembled lithium

symmetric batteries demonstrated stable cycling for over 3000 h at a low polarization voltage of 0.015 V, with a critical current density (CCD) as high as 2.8 mA cm^{-2}. Through EIS, EDS, TOF-SIMS, and XPS etching, a unique LiCl/Li$_3$N gradient interfacial layer was identified to form during cycling. Benefiting from enhanced anode interface stability, ASSBs integrating N-doped LZC with LiCoO$_2$ cathodes and Li–In anodes demonstrate exceptional rate capability, delivering 142 mAh g^{-1} and 218 mAh g^{-1} at 0.1C when charged to 4.22 V and 4.62 V (*vs.* Li$^+$/Li), respectively, surpassing those of most reported halide-based ASSBs to date.

Results and discussion

Material characterization and analysis

A series of nitrogen–halide solid electrolytes Li$_{2+2x}$ZrCl$_{6-x}$N$_x$ (LZC-Nx, x = 0, 0.05, 0.1, 0.15, 0.2, and 0.25) were synthesised in this work *via* high-energy ball milling of stoichiometrically controlled LiCl, ZrCl$_4$, and Li$_3$N precursors. Fig. 1a displays the powder XRD patterns, revealing that LZC-Nx retains a crystal structure highly analogous to pristine LZC (space group: $P\bar{3}m1$) with a hexagonally close-packed anionic framework at low N-doping levels (x ≤ 0.15). The gradual attenuation of three dominant peaks at 16.3°, 32.0°, and 41.8° with increasing x signifies enhanced amorphization induced by nitrogen incorporation. Concurrently, intensified peaks at 29.8° and 34.5° for x ≥ 0.2 indicate phase transitions or impurity formation under excessive doping. Detailed analysis of the (041) peak at 32.0° demonstrates systematic low-angle shifting with higher x values, demonstrating nitrogen-doping-induced lattice expansion. Raman analysis provides molecular vibration evidence for nitrogen-doping-driven structural evolution. As shown in Fig. 1b, LZC-Nx samples with x ≤ 0.15 exhibit Raman spectral features closely matching those of pristine LZC, with characteristic vibration modes at 326 cm^{-1} and 163 cm^{-1} corresponding to the A$_{1g}$ stretching and F$_{2g}$ bending vibrations of ZrX$_6$ (X = Cl and N) octahedral coordination.[14] However, at x ≥ 0.2, significant spectral shifts accompanied by peak broadening are observed, attributable to the collapse of ZrX$_6$ octahedral structures caused by excessive nitrogen doping.

The ionic conductivities of the synthesized nitrogen–halide SEs were systematically evaluated. As shown in Fig. 1c, the ionic conductivity exhibits a volcano-shaped trend with increasing doping content, where pristine LZC exhibits a room-temperature conductivity of 0.51 mS cm^{-1}, comparable to the average levels reported in the literature.[11,13,15] N-doped LZC-N0.05, LZC-N0.1, LZC-N0.15, LZC-N0.2, and LZC-N0.25 achieve conductivities of 0.93, 1.18, 1.50, 1.34, and 0.74 mS cm^{-1}, respectively, peaking at x = 0.15 with a near twofold enhancement over undoped LZC. LZC-N0.15 exhibits a substantially reduced Li$^+$ migration activation energy (0.244 eV) compared to pristine LZC (0.349 eV), as demonstrated in Fig. 1d, indicating lowered diffusion barriers through lattice engineering. DC polarization measurements reveal that minimal N-doping (x = 0.05) decreases electronic conductivity from 8.50 × 10^{-10} S cm^{-1} to 5.08 × 10^{-10} S cm^{-1}, with further
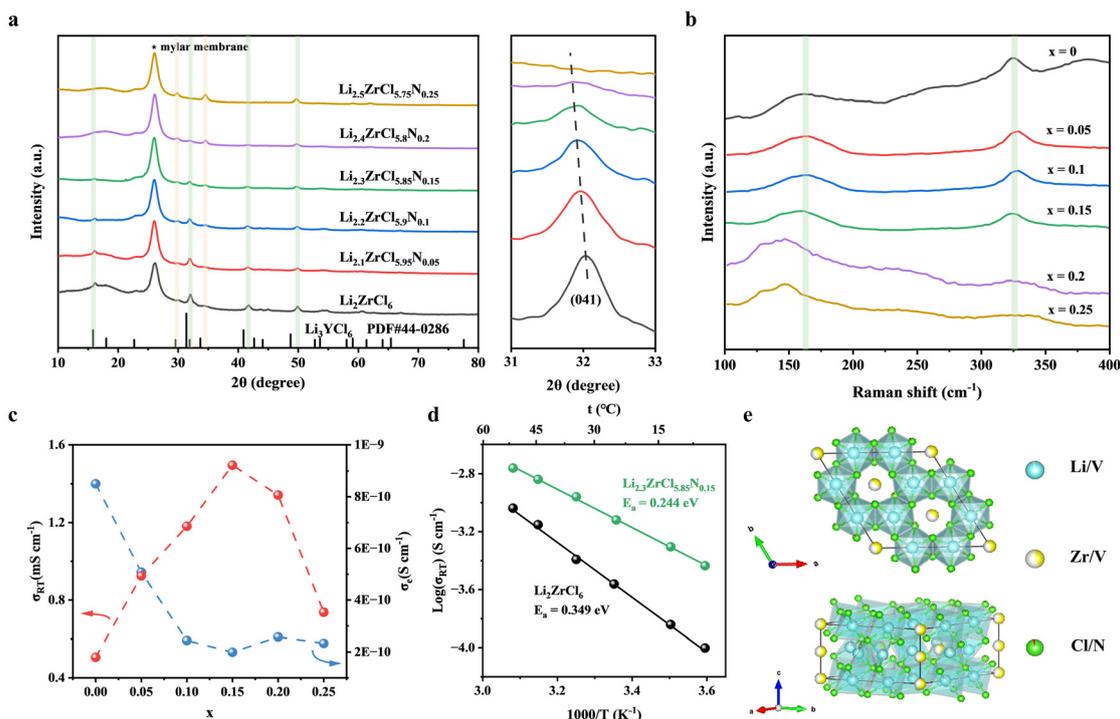
Fig. 1 (a) XRD patterns and (b) Raman spectra of LZC-Nx. (c) Ionic/electronic conductivity trends of LZC-Nx as a function of nitrogen-doping level. (d) Activation energy measurement results of LZC and LZC-N0.15. (e) Refined crystal structure of LZC-N0.15 derived from XRD Rietveld data, with Li, Zr, Cl, and N atoms depicted in cyan, yellow, green, and red, respectively. V denotes a vacancy.

reduction to ~2×10^{-10} S cm^{-1} at $x \geq 0.1$. N-doping synergistically optimizes ionic/electronic transport properties, with LZC-N0.15 demonstrating the best overall performance: the highest ionic conductivity (1.50 mS cm^{-1}) and the lowest electronic conductivity (1.99×10^{-10} S cm^{-1}).

XPS analysis was employed to characterize the elemental oxidation states and bonding configurations within the LZC-Nx electrolytes, with the results presented in Fig. S3.† In the Li 1s spectrum of pristine LZC, the peak at 56.41 eV is attributed to lithium within the electrolyte component (SE–Li), while the peak at 54.21 eV is assigned to the Zr 4s orbital of LZC (SE–Zr).[15] For LZC-N0.15, while the Zr 4s signal does not show any significant change, the Li 1s spectrum exhibits notable differences: a new peak emerges at 55.96 eV, distinct from the Li$_3$N reference peak at 54.56 eV.[16] This observation supports the successful incorporation of nitrogen into Cl$^-$ sites in the electrolyte structure. Concurrently, the original SE–Li peak shifts to a higher binding energy (56.65 eV) with reduced intensity, which may be attributed to decreased electron cloud density around Li atoms and partial transition from Cl-coordinated to N-coordinated Li sites. In the Zr 3d spectra, both LZC and LZC-N0.15 display spin–orbit splitting peaks at 183.36 eV (Zr 3d5/2) and 185.74 eV (Zr 3d3/2), matching standard Zr^{4+} reference data,[13] demonstrating preserved zirconium oxidation states under moderate N-doping conditions.

To further elucidate the relationship between N-doping-induced structural evolution and enhanced ionic conductivity, Rietveld refinement of XRD data was performed, enabling the

construction of a refined crystal structure model. As shown in Fig. 1e, the LZC-N0.15 crystal adopts a hexagonal closest packing arrangement, with an anion framework composed of Cl$^-$ and N^{3-} ions. Nitrogen selectively occupies three distinct crystallographic sites originally belonging to Cl$^-$ (Cl1, Cl2, and Cl3) with occupancy rates of 1.15%, 2.97%, and 5.11%, respectively. Anions form octahedral coordination environments around the central cations, creating a regular honeycomb network structure in the ab-plane with pore centers occupied by Zr^{4+}, Li$^+$, or vacancies. Compared to pristine LZC ($a = b = 11.053$ Å and $c = 5.962$ Å), LZC-N0.15 exhibits significantly expanded lattice parameters ($a = b = 11.145$ Å and $c = 6.042$ Å) and an increased unit cell volume (650.015 Å^3 $vs.$ 630.739 Å^3 for LZC). This volume expansion likely originates from lattice distortion caused by the ionic radius difference between N^{3-} and Cl$^-$, coupled with enhanced electrostatic interactions from N^{3-} incorporation.

To investigate the influence of nitrogen doping on the local chemical environments of lithium, ^{7}Li ssNMR analysis was conducted on LZC-Nx. The ^{7}Li ssNMR spectrum of pristine LZC exhibits an asymmetric peak profile (Fig. S5†), deconvoluted into a main peak at −0.847 ppm and a shoulder at −1.254 ppm. The latter aligns with the chemical shift of standard LiCl, indicating an incomplete reaction of LiCl during synthesis. In contrast, the LZC-N0.15 spectrum (Fig. 2a) displays a symmetric peak at −0.506 ppm, showing distinct differences from standard LiCl (−1.254 ppm) and Li$_3$N (7.184 ppm), confirming that Li$_3$N is not present as a separate phase but incorporated into the crystal
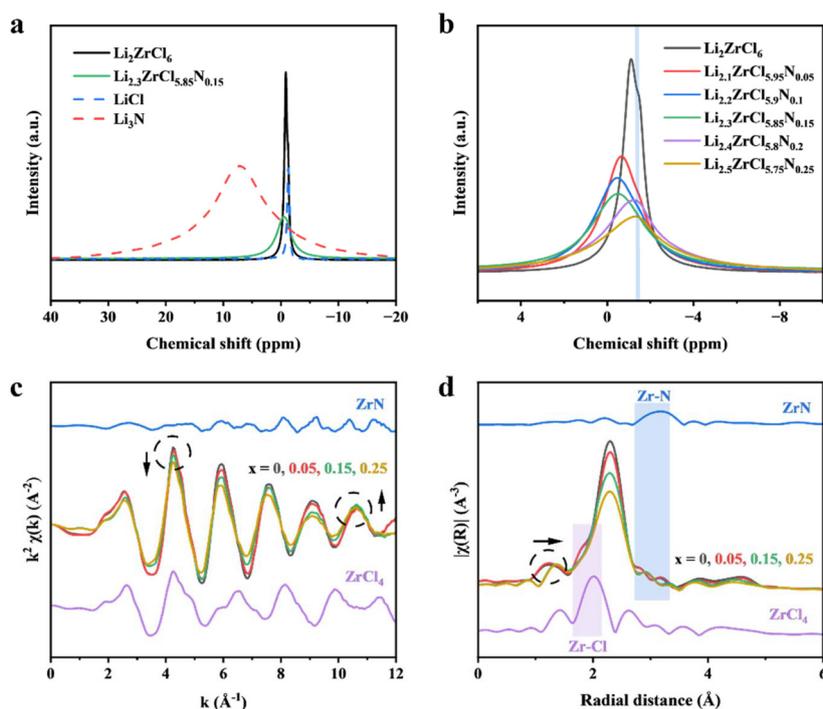
Fig. 2 (a) The ^7Li ssNMR spectra of LZC, LZC-N0.15, LiCl, and Li_3N. (b) Evolution of ^7Li ssNMR spectral features in LZC-Nx with increasing N-doping levels. (c) K-space and (d) R-space of the XAS spectra of LZC, LZC-N0.05, LZC-N0.15, LZC-N0.25, ZrN, and $ZrCl_4$.

lattice. Nitrogen-doping levels significantly modulate the ^7Li ssNMR profiles of LZC-Nx. As shown in Fig. 2b, the intensity of LiCl impurity peaks becomes barely detectable at x = 0.05 and disappears completely when $x \geq 0.1$. Additionally, the chemical shift of the main peak gradually increases with rising doping levels when $x \leq 0.15$. This is because N^{3-} possesses a higher charge density compared to Cl^-, creating a stronger local electric field that enhances the paramagnetic deshielding effect on the Li^+ nucleus, whereas a sharp decrease occurs at $x \geq 0.2$, suggesting a critical doping threshold between x = 0.15 and x = 0.2, beyond which drastic changes occur in the local lithium environment, correlating with structural degradation observed by XRD and Raman. The reduced symmetry of Li^+ sites and increased amorphization drive the chemical shift downfield. Further analysis of peak linewidth evolution reveals that increased N-doping induces a transition toward broader Gaussian-type linewidth characteristics. This spectral broadening reflects progressive disordering of the lithium local environment, likely arising from lattice defects and structural heterogeneity introduced by nitrogen incorporation. Integration of peak areas for LZC-N0.15 and LZC, after correcting for LiCl impurity contributions in LZC, yields a lithium-ion concentration ratio of 1.146. This ratio closely matches the theoretical stoichiometric ratio ($Li_{2.3}ZrCl_{5.85}N_{0.15}$ vs. Li_2ZrCl_6), confirming that doping elevates the lithium stoichiometric number, thereby enhancing the ionic conductivity.

Given the highly amorphous nature of the synthesized LZC-Nx, we employed Zr K-edge X-ray absorption spectroscopy to investigate LZC-Nx (x = 0, 0.05, 0.15, 0.25). As shown in

Fig. S6,† all samples exhibit high similarity to crystalline $ZrCl_4$, suggesting structural homology in the local $[ZrCl_6]^{2-}$ octahedral coordination. K-space analysis (Fig. 2c) reveals systematic attenuation of oscillation amplitudes with increasing x, indicative of enhanced Zr–X (X = Cl/N) coordination disorder and reduced average coordination numbers. However, the oscillation intensity at k = 10.6 Å^{-1} anomalously increases for higher-doped LZC-N0.15 and LZC-N0.25. Wavelet analysis of ZrN references (Fig. S7†) attributes this feature to Zr–N bonding, confirming successful incorporation of nitrogen coordination. R-space analysis (Fig. 2d) shows progressive reduction of the first coordination shell peak intensity with increasing x, consistent with decreasing Cl coordination numbers. In highly doped samples (x = 0.15 and 0.25), diminished Zr–Cl features at ~2 Å and inverted wave patterns compared to low-doped samples (x = 0 and 0.05) at 3 Å provide further evidence for Zr–N coordination formation. Additionally, a rightward shift of the 1.3 Å minor peak in high-doped samples correlates with increased amorphousness, suggesting local bond elongation due to altered Zr site symmetry or crystalline defects. Wavelet transform decoupling (Fig. S8†) reveals systematic suppression of second-shell Cl–Zr–Cl signals ($R \approx 4$ Å) alongside enhanced k-space intensity at higher wavevectors, suggesting localized Cl–Zr–N configurations. Concurrently, the intensified wavelet modulus at $R \approx 1$ Å with doping aligns with ZrN spectral fingerprints. This spectroscopic evidence collectively verifies that N-doping progressively substitutes Cl sites in $[ZrCl_6]^{2-}$ octahedra, forming disordered $[ZrCl_{6-x}N_x]^{2-}$ units. Such coordination disorder

amplifies the amorphous character, which facilitates rapid ion transport through decoupled charge carrier pathways within the structurally relaxed matrix.[17,18]

By integrating these characterization results with ionic conductivity measurements, we conclude that the enhanced ionic conductivity of LZC-N0.15 arises synergistically from lattice expansion, increased Li$^+$ stoichiometric number, and amorphous phase formation. Previous studies have demonstrated that LZC facilitates Li$^+$ migration through a three-dimensional transport network comprising c-axis O–O pathways and ab-plane O–T–O interconnections.[13] The observed lattice expansion broadens migration bottlenecks within the network. Concurrently, the elevated Li$^+$ stoichiometric number directly amplifies charge carrier content, and the amorphous phase promotes decoupling of ion transport pathways from the rigid structural framework.

The morphological evolution of LZC-Nx powders with varying doping levels was investigated by SEM. As shown in Fig. 3a, all samples are irregular secondary micron-sized particles composed of primary nanoparticles. Progressive N-doping induces increased particle agglomeration, with the particle size gradually expanding from 1–4 μm, suggesting enhanced interparticle adhesion induced by nitrogen incorporation. EDS (Fig. S9†) confirms the homogeneous distribution of Zr, Cl, and N elements in the LZC-N0.15 sample. Under identical compaction pressures, pellets fabricated from LZC and LZC-N0.15 powders exhibited distinct surface morphologies (Fig. 3b). The LZC-N0.15 pellet demonstrated significantly reduced surface porosity and a denser microstructure compared to LZC, indicating enhanced densification upon N-doping, which correlates with strengthened interparticle adhesion and increased amorphous content, promoting improved interfacial contact between electrolyte particles and at electrolyte/electrode interfaces.

LSV revealed the electrochemical stability window. As shown in Fig. 3c and d, LZC exhibited a stability window of 1.76–4.03 V, while N-doping expanded this range to 1.69–4.08 V. A magnified view (inset of Fig. 3c) shows a minor oxidation peak at ~3.6 V in LZC-N0.15, attributed to sacrificial oxidation of N^{3-} species. This self-limiting reaction delays the chloride oxidation onset, resulting in lower oxidation currents than LZC. Notably, the oxidation current decreased beyond 4.55 V, likely due to passivation layer formation. During reduction scans, LZC-N0.15 exhibits slightly negative-shifted reduction potentials relative to LZC but maintains significant reduction currents, consistent with the intrinsic reduction instability associated with Zr^{4+}. While N-doping cannot fundamentally alter this intrinsic property, it substantially suppresses Zr^{4+} kinetic reduction, as evidenced by the attenuated reduction peak at 0.88 V.

Electrochemical performance of all-solid-state lithium batteries

Electrochemical performance testing of ASSBs based on LZC-N0.15, employing LiCoO$_2$ (LCO) as the active cathode material and a LiIn alloy (0.62 V $vs.$ Li$^+$/Li) as the anode, demonstrated superior electrochemical performance compared to their LZC-based counterparts. As shown in Fig. 4a, at room temperature and 0.1C, LCO/LZC-N0.15/LiIn achieved a first-cycle discharge specific capacity of 141.7 mAh g^{-1} with an exceptional initial coulombic efficiency (ICE) of 96.9%, whereas LCO/LZC/LiIn exhibited a lower discharge capacity of 128.5 mAh g^{-1} and an ICE of 93.3%. This enhancement stems from reduced polarization, evidenced
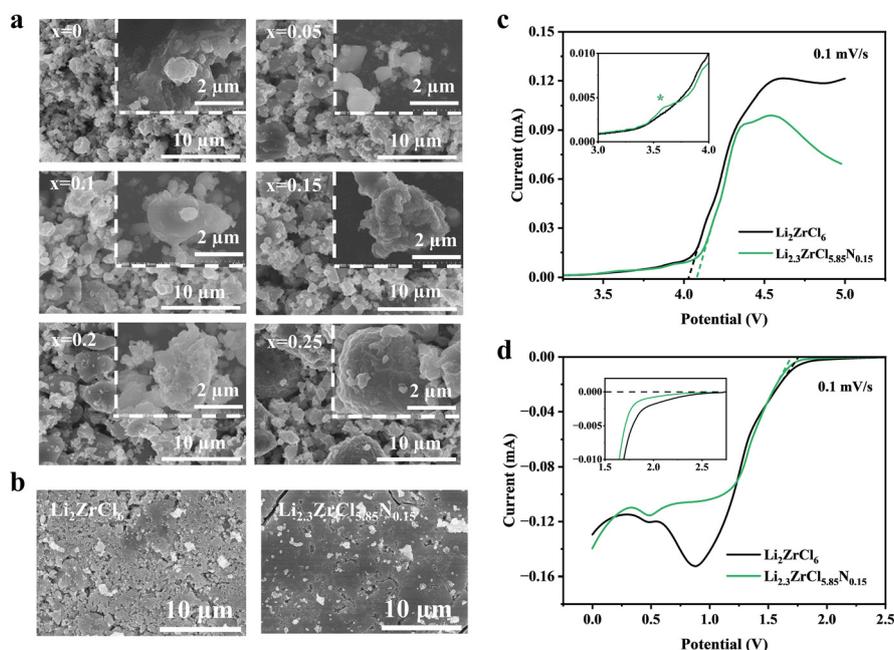

Fig. 3 (a) SEM images of LZC-Nx electrolyte powders. (b) SEM images of LZC and LZC–N0.15 electrolyte pellets. LSV curves for (c) the positive scan and (d) the negative scan of LZC and LZC–N0.15.
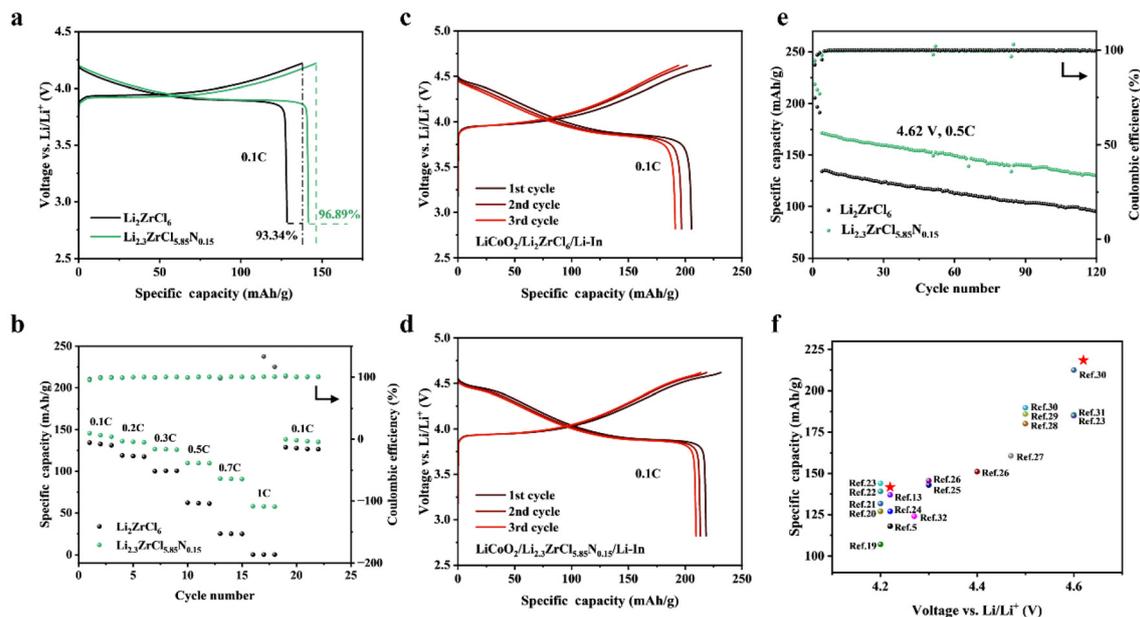
Fig. 4 (a) Initial charge–discharge curves of LCO/LZC/LiIn and LCO/LZC-N0.15/LiIn and (b) rate capability tests at various rates charged to 4.22 V (vs. Li$^+$/Li). (c and d) First three-cycle charge–discharge curves of LCO/LZC/LiIn and LCO/LZC-N0.15/LiIn and (e) cycling performance at 0.5C under 4.62 V cutoff voltage. (f) Comparison of discharge specific capacities and upper cutoff voltages between this work and previously reported LCO/halide-based ASSBs.[5,13,19–32]

by lower charge plateaus and higher discharge plateaus in LZC-N0.15, attributable to its superior ionic conductivity, improved electrode–electrolyte interfacial contact, and enhanced electrochemical stability. Rate capability tests (Fig. 4b) demonstrated remarkable improvements. At 1C, LCO/LZC-N0.15/LiIn maintained 58.0 mAh g^{-1}, while LZC exhibited negligible capacity. These results indicate severe polarization in LCO/LZC/LiIn, which is predominantly caused by interfacial instability, as the dominant polarization source at high rates. Long cycling (Fig. S10†) revealed 79.0% capacity retention for LCO/LZC-N0.15/LiIn after 150 cycles at 0.5C, compared to 70.3% for LZC. To further validate the compatibility of LZC-N0.15 in high-voltage cathodes, electrochemical tests were extended to a cutoff voltage of 4.62 V. Fig. 4c and d compare the first three charge/discharge cycles at 0.1C and LCO/LZC/LiIn exhibited significant polarization and rapid capacity decay (205.5, 196.8, and 191.3 mAh g^{-1}) with a 92.3% ICE, while LCO/LZC-N0.15/LiIn exhibited higher capacities (218.4, 213.4, and 209.7 mAh g^{-1}) and an improved ICE of 94.3%. At 4.62 V, LCO/LZC-N0.15/LiIn exhibits capacity decay due to aggravated interfacial side reactions, LCO phase transitions, and contact loss, yet outperforms LCO/LZC/LiIn. After 120 cycles at 0.5C, its capacity retention improves from 71.0% to 75.8% despite higher capacity. As summarized in Fig. 4f, this work achieves superior discharge capacities among reported LCO/halide-based ASSBs at both 4.22 V and 4.62 V.[5,13,19–32]

Electrolyte/lithium metal interface stability

Given the intrinsic high-voltage stability of metal chloride SEs, the significant performance disparity between LCO/LZC/LiIn and LCO/LZC-N0.15/LiIn under high-rate conditions is primar-

ily attributed to anode interfacial dynamics. Lithium symmetric batteries were thus assembled to investigate the impact of N-doping levels on electrolyte–lithium stability (Fig. 5a). Galvanostatic cycling at 0.1 mA cm^{-2} revealed that Li/LZC/Li exhibited the highest polarization voltage with pronounced voltage fluctuations, indicative of lithium dendrite growth and interfacial micro-shorting. In contrast, LZC-Nx demonstrated reduced polarization and more stable Li plating/stripping profiles. At $x = 0.05$, polarization voltage modestly decreased but remained elevated. For $x = 0.1$, the initial polarization dropped significantly and stable cycling was sustained for over 3600 hours, albeit with a gradual voltage creep. Optimal performance emerged at $x = 0.15$, where symmetric batteries sustained an ultralow polarization of 0.015 V over 3000 h without voltage drift. However, excessive doping ($x = 0.25$) increased initial polarization, followed by abrupt voltage spikes after ~500 h. These results suggest that moderate N-doping ($x = 0.15$) optimally balances interfacial stability and ionic conductivity. At low doping levels ($x \leq 0.1$), interfacial reactions generate thick, unstable interphases, causing progressive polarization growth. At high doping levels ($x \geq 0.2$), structural degradation and impurity phases reduce ionic conductivity, exacerbating interfacial instability. Notably, all batteries exhibited an initial polarization surge followed by stabilization, termed stage I and stage II. In stage I, the polarization voltage increases rapidly due to inherent interfacial defects and vigorous reactions between the halide electrolyte and lithium metal. These reactions initially degrade the contact at the Li/LZC-Nx interface. However, the decomposition of the electrolyte also produces nitrogen-containing species, which accumu-
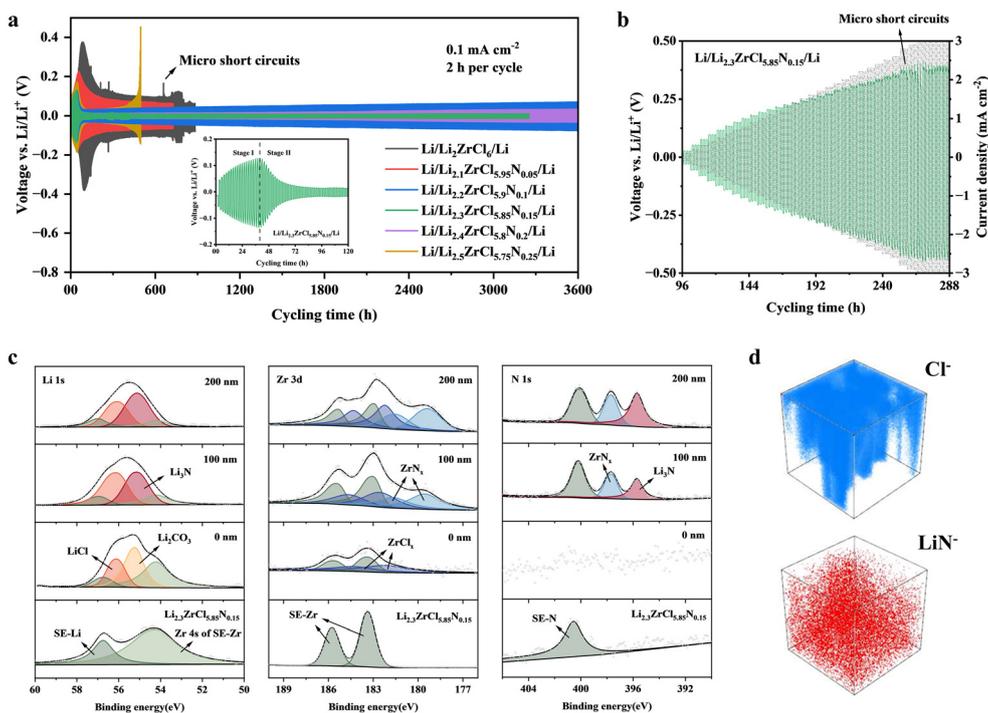
Fig. 5 (a) Stripping/plating cycling curves of Li/LZC-Nx/Li at 0.1 mA cm^{-2} and a magnified view of the initial-stage Li/LZC-N0.15/Li. (b) CCD test for Li/LZC-N0.15/Li. (c) XPS fitting results of the LZC-N0.15 electrolyte and the Li/LZC-N0.15 interphase at different etching depths. (d) 3D rendering of spatial distribution for Cl^{-} and LiN^{-} fragments within the Li/LZC-N0.15 interphase layer.

late at the interface to form a self-limiting protective layer. The layer suppresses continuous decomposition and guides uniform lithium deposition, effectively filling interfacial voids and increasing the electroactive contact area. As the opposing effects of the interfacial reaction (which increases polarization) and increasing contact area (which decreases polarization) reach a dynamic balance, the battery transitions to stage II. During this phase, the polarization voltage gradually declines and eventually stabilizes. Once the self-limiting interphase is fully formed, interfacial reactions are essentially suppressed, enabling long-term cycling at a constant low polarization voltage. Similar self-healing interfacial behavior has been reported in previous studies.[15,33]

To evaluate the limit of lithium stripping/plating areal capacity performance for LZC-N0.15, critical current density (CCD) testing was conducted. As shown in Fig. 5b, after the activation stage of Li/LZC-N0.15N/Li, stepwise increases in current density induced corresponding polarization voltage escalation. A distinct voltage drop occurred at 2.8 mA cm^{-2}, indicating partial lithium dendrite penetration through the electrolyte. As shown in Fig. S11,† this CCD is competitive with those of state-of-the-art anode-modified electrolytes. Notably, the polarization voltage increase remained sublinear with respect to the rising current density, particularly under high-rate conditions. This behavior can be attributed to the *in situ* formation of a nitrogen-rich interphase layer, which possesses low interfacial energy with lithium. As a result, deposited lithium can infiltrate into the interfacial region, increasing the

effective contact area and thereby mitigating voltage buildup. At high areal capacities, lithium infiltration into interfacial voids becomes more pronounced, further enhancing interfacial contact and contributing to the stabilized, gradual increase in polarization voltage as observed in previous studies.[34,35] Fig. S12† illustrates the cycling behavior of Li/LZC-N0.15/Li at 0.5 mA cm^{-2} with 0.5 mAh cm^{-2} areal capacity, revealing analogous activation stages but higher stabilized polarization (~0.184 V) over 700 h of stable operation.

To thoroughly investigate the stabilization mechanism of the interface between lithium metal and LZC-N0.15, we employed EIS, EDS, TOF-SIMS, and XPS to analyze the *in situ* formed interfacial layer. Fig. S13† illustrates the impedance evolution of Li/LZC/Li and Li/LZC-N0.15/Li during 15-day storage. Freshly assembled Li/LZC/Li exhibited dual semicircles in high- and mid-frequency regions, corresponding to grain boundary and interfacial resistances, whereas Li/LZC-N0.15/Li showed only a high-frequency semicircle, indicating suppressed interfacial reactivity by N-doping. However, inherent thermodynamic instability between halide electrolytes and lithium drove continued interfacial reactions, a rapid increase peaking on day 2 (1440 Ω for Li/LZC-N0.15/Li and 2230 Ω for Li/LZC/Li) due to aggressive chemical reactions and deteriorated physical contact. While Li/LZC-N0.15/Li reached stable impedance after 10 days, Li/LZC/Li required over 15 days for partial stabilization. Notably, the final interfacial impedance of Li/LZC-N0.15/Li was significantly lower than that of Li/LZC/Li. These results demonstrate that N-doping

accelerates passivation layer formation kinetics, minimizes interfacial damage, and optimizes interphase composition, resulting in lower overall impedance.

Post-mortem analysis was conducted on Li/LZC/Li and Li/LZC-N0.15/Li symmetric batteries cycled for 200 h at 0.1 mA cm^{-2} and 0.1 mAh cm^{-2}. EDS mapping of the Li/LZC-N0.15 interface (Fig. S14†) revealed a uniform nitrogen-rich layer covering the lithium surface. In contrast to the EDS results from pristine LZC-N0.15 particles (Fig. S8†), the interfacial layer showed depleted Zr and Cl signals compared to the N signal, suggesting the *in situ* formation of an N-enriched interphase during cycling. Lithiophilic nitrogen species preferentially deposit on lithium metal, while Zr- and Cl-containing reaction products accumulate on the electrolyte side. Conversely, the Li/LZC interface contained only Zr and Cl species, with direct contact between zirconium-rich phases and lithium metal, which is detrimental to interfacial stability. To further elucidate the compositional evolution of Li/LZC-N0.15 interphase post-cycling, XPS depth profiling was performed, analyzing the interphase at etching depths of 0 nm, 100 nm, and 200 nm. The fitted results are presented in Fig. 5c. In the Li 1s spectra, two peaks from the LZC-N0.15 electrolyte were assigned to SE–Li (56.74 eV) and Zr 4s (54.21 eV)[15] and contributions from Li–Cl and Li–N bonding to the SE–Li signal were not differentiated here. At the surface (0 nm), characteristic electrolyte peaks coexisted with LiCl (56.09 eV)[36] and Li$_2$CO$_3$ (55.22 eV),[37] with the latter arising from air exposure during sample handling. With increasing depth, Li$_2$CO$_3$ diminished, while electrolyte signatures decreased. At 100 nm, Li$_3$N (55.13 eV)[38] emerged, intensifying at 200 nm alongside reduced LiCl concentrations. Similar trends are observed in Zr 3d and N 1s spectra. The pristine electrolyte's doublet (183.36 eV for Zr 3d5/2 and 185.74 eV for Zr 3d3/2) persisted at 0 nm, accompanied by ZrCl$_x$ peaks (182.55 eV and 184.62 eV).[15] Deeper etching introduced ZrN$_x$ signatures (179.55 eV and 181.65 eV),[39] with ZrN$_x$ concentration increasing at 200 nm. In the N 1s spectra, the peak at 400.56 eV corresponds to the LZC-N0.15 electrolyte. At the surface (0 nm), no nitrogen signal was detected due to low nitrogen concentration and potential air contamination. After etching, additional peaks emerged at 397.70 eV (ZrN$_x$)[40] and 395.71 eV (Li$_3$N),[16] with nitrogen-containing species showing significantly increased concentrations at greater depths. These results conclusively demonstrate the *in situ* formation of Li$_3$N within the interphase, with LiCl localized near the electrolyte and lithiophilic Li$_3$N enriched in the inner interface layer. TOF-SIMS was employed to analyze the depth-dependent distribution of Cl$^-$ and LiN$^-$ fragments within the interphase, with the results shown in Fig. S15.† In the Li/LZC interphase, Cl$^-$ exhibited uniform intensity with minimal depth dependence, while LiN$^-$ signals remained negligible. Conversely, Li/LZC-N0.15 displayed anticorrelated Cl$^-$/LiN$^-$ trends: the Cl$^-$ intensity rapidly attenuated near the electrolyte surface, plateauing at lower values with progressive sputtering, whereas LiN$^-$ signals intensified toward deeper regions. This selective distribution is visually confirmed in the 3D renderings (Fig. 5d).

The TOF-SIMS results align with EDS and XPS depth profiling, further validating the spatially resolved segregation of Cl-containing species (*e.g.*, LiCl) toward the electrolyte side and N-containing species (*e.g.*, Li$_3$N) toward the lithium metal side, forming a gradient interphase. The driving force for this component segregation likely stems from the differing lithiophilicity of L$_3$N and LiCl. Li$_3$N, possessing low interfacial energy with lithium, preferentially deposits on the lithium side,[41,42] creating a nitrogen-rich interphase. This gradient interphase offers dual benefits: (1) lithiophilic Li$_3$N guides uniform lithium plating/stripping and increases the effective contact area through partial lithium infiltration, reducing polarization, and (2) the electrolyte-adjacent LiCl-rich layer with low electronic conductivity acts as a physical barrier to suppress continuous lithium penetration.[43]

Conclusions

In this work, we successfully synthesized nitrogen–halide electrolytes LZC-Nx. The optimized LZC-N0.15 exhibits a near twofold enhancement in ionic conductivity (1.5 mS cm^{-1}) compared to pristine LZC (0.51 mS cm^{-1}). Multiple characterization techniques revealed that this enhancement arises from a synergistic effect of lattice expansion, increased lithium stoichiometry, and amorphization. ASSBs integrating LZC-N0.15 with LCO cathodes and LiIn anodes demonstrated exceptional electrochemical performance. When charged to 4.22 V, the battery delivered a first-cycle discharge capacity of 141.7 mAh g^{-1} and 96.9% ICE at 0.1C, alongside significantly improved rate capability. Raising the cutoff voltage to 4.62 V enabled a high discharge capacity of 218.4 mAh g^{-1} with 94.3% ICE, surpassing most previously reported halide-based systems. The enhanced anode stability, evidenced by a CCD of 2.8 mA cm^{-2}, stems from an *in situ*-formed LiCl/Li$_3$N gradient interphase. This architecture features lithiophilic Li$_3$N enriched on the Li metal side to guide uniform deposition, coupled with LiCl near the electrolyte to suppress lithium penetration, embodying a unique structure–function integration paradigm.

Author contributions

The manuscript was written through the contributions of all authors. All authors have approved the final version of the manuscript. Y. Deng: conceptualization, data curation, formal analysis, investigation, methodology, visualization, writing – original draft, and writing – review & editing. Z. Liang: conceptualization and methodology. R. Ma: methodology and writing – review & editing. Y. Zhou: methodology. Y. Su: methodology. W. Huang: methodology. S. Pan: methodology. Y. Luo: methodology. Z. Qin: methodology. Y. Chen: methodology. Z. Gong: methodology. Y. Yang: conceptualization, funding acquisition, project administration, supervision, validation, visualization, and writing – review & editing.

Conflicts of interest

The authors declare no conflict of interest.

Data availability

All data generated or analyzed during this study are included in this article and the ESI.†

Acknowledgements

References

1 P. Bonnick and J. Muldoon, *Energy Environ. Sci.*, 2022, **15**, 1840–1860.

2 Y. Duan, X. Bai, T. Yu, Y. Rong, Y. Wu, X. Wang, J. Yang and J. Wang, *J. Energy Storage*, 2022, **55**, 105382.

3 S. Jian, H. Li, X. Jia, D. Zhong, B. Tao, X. He, G. Wang and H. Chang, *FlatChem*, 2024, **46**, 100693.

4 X. Lu, Y. Wang, X. Xu, B. Yan, T. Wu and L. Lu, *Adv. Energy Mater.*, 2023, **13**, 2301746.

5 T. Asano, A. Sakai, S. Ouchi, M. Sakaida, A. Miyazaki and S. Hasegawa, *Adv. Mater.*, 2018, **30**, 1803075.

6 X. Li, J. Liang, X. Yang, K. R. Adair, C. Wang, F. Zhao and X. Sun, *Energy Environ. Sci.*, 2020, **13**, 1429–1461.

7 T. Krauskopf, F. H. Richter, W. G. Zeier and J. Janek, *Chem. Rev.*, 2020, **120**, 7745–7794.

8 Y. Fu and C. Ma, *Sci. China Mater.*, 2021, **64**, 1378–1385.

9 L. M. Riegger, R. Schlem, J. Sann, W. G. Zeier and J. Janek, *Angew. Chem., Int. Ed.*, 2021, **60**, 6718–6723.

10 C. Rosenbach, F. Walther, J. Ruhl, M. Hartmann, T. A. Hendriks, S. Ohno, J. Janek and W. G. Zeier, *Adv. Energy Mater.*, 2022, **13**, 2203673.

11 W. Tang, W. Xia, F. Hussain, J. Zhu, S. Han, W. Yin, P. Yu, J. Lei, D. S. Butenko, L. Wang and Y. Zhao, *J. Power Sources*, 2023, **568**, 232992.

12 X. Xu, G. Du, C. Cui, J. Liang, C. Zeng, S. Wang, Y. Ma and H. Li, *ACS Appl. Mater. Interfaces*, 2022, **14**, 39951–39958.

13 K. Wang, Q. Ren, Z. Gu, C. Duan, J. Wang, F. Zhu, Y. Fu, J. Hao, J. Zhu, L. He, C.-W. Wang, Y. Lu, J. Ma and C. Ma, *Nat. Commun.*, 2021, **12**, 4410.

14 H. Kwak, D. Han, J. Lyoo, J. Park, S. H. Jung, Y. Han, G. Kwon, H. Kim, S.-T. Hong, K.-W. Nam and Y. S. Jung, *Adv. Energy Mater.*, 2021, **11**, 2003190.

15 X. Luo, X. He, H. Su, Y. Zhong, X. Wang and J. Tu, *Chem. Eng. J.*, 2023, **465**, 143036.

16 K. N. Wood and G. Teeter, *ACS Appl. Energy Mater.*, 2018, **1**, 4493–4504.

17 J. L. Souquet, *Annu. Rev. Mater. Res.*, 1981, **11**, 211–231.

18 C. A. Angell, *Annu. Rev. Phys. Chem.*, 1992, **43**, 693–717.

19 T. Ma, Z. Wang, D. Wu, P. Lu, X. Zhu, M. Yang, J. Peng, L. Chen, H. Li and F. Wu, *Energy Environ. Sci.*, 2023, **16**, 2142–2152.

20 Y. Tanaka, K. Ueno, K. Mizuno, K. Takeuchi, T. Asano and A. Sakai, *Angew. Chem., Int. Ed.*, 2023, **62**, e202217581.

21 C. Wang, J. Liang, M. Jiang, X. Li, S. Mukherjee, K. Adair, M. Zheng, Y. Zhao, F. Zhao, S. Zhang, R. Li, H. Huang, S. Zhao, L. Zhang, S. Lu, C. V. Singh and X. Sun, *Nano Energy*, 2020, **76**, 105015.

22 C. Wang, J. Liang, J. Luo, J. Liu, X. Li, F. Zhao, R. Li, H. Huang, S. Zhao, L. Zhang, J. Wang and X. Sun, *Sci. Adv.*, 2021, **7**, eabh1896.

23 Z. Song, T. Wang, H. Yang, W. H. Kan, Y. Chen, Q. Yu, L. Wang, Y. Zhang, Y. Dai, H. Chen, W. Yin, T. Honda, M. Avdeev, H. Xu, J. Ma, Y. Huang and W. Luo, *Nat. Commun.*, 2024, **15**, 1481.

24 X. Li, J. Liang, J. Luo, M. Norouzi Banis, C. Wang, W. Li, S. Deng, C. Yu, F. Zhao, Y. Hu, T.-K. Sham, L. Zhang, S. Zhao, S. Lu, H. Huang, R. Li, K. R. Adair and X. Sun, *Energy Environ. Sci.*, 2019, **12**, 2665–2671.

25 L. Zhou, C. Y. Kwok, A. Shyamsunder, Q. Zhang, X. Wu and L. F. Nazar, *Energy Environ. Sci.*, 2020, **13**, 2056–2063.

26 L. Hu, J. Wang, K. Wang, Z. Gu, Z. Xi, H. Li, F. Chen, Y. Wang, Z. Li and C. Ma, *Nat. Commun.*, 2023, **14**, 3807.

27 S. Zhang, F. Zhao, S. Wang, J. Liang, J. Wang, C. Wang, H. Zhang, K. Adair, W. Li, M. Li, H. Duan, Y. Zhao, R. Yu, R. Li, H. Huang, L. Zhang, S. Zhao, S. Lu, T.-K. Sham, Y. Mo and X. Sun, *Adv. Energy Mater.*, 2021, **11**, 2100836.

28 Y. Gao, S. Zhang, F. Zhao, J. Wang, J. Zhou, W. Li, S. Deng, J. Fu, X. Hao, R. Li and X. Sun, *ACS Energy Lett.*, 2024, **9**, 1735–1742.

29 H. Kwak, J.-S. Kim, D. Han, J. S. Kim, J. Park, G. Kwon, S.-M. Bak, U. Heo, C. Park, H.-W. Lee, K.-W. Nam, D.-H. Seo and Y. S. Jung, *Nat. Commun.*, 2023, **14**, 2459.

30 H.-S. Zhang, X.-C. Lei, D. Su, S.-J. Guo, J.-C. Zhu, X.-F. Wang, X. Zhang, T.-T. Wu, S.-Q. Lu, Y.-T. Li and A.-M. Cao, *Angew. Chem., Int. Ed.*, 2024, **63**, e202400562.

31 Z. Wang, J. Tan, Z. Jia, J. Cui, X. Wang, C. Shu, X. Gao, Y. Wu and W. Tang, *ACS Energy Lett.*, 2024, **9**, 4485–4492.

32 Z. Liu, S. Ma, J. Liu, S. Xiong, Y. Ma and H. Chen, *ACS Energy Lett.*, 2021, **6**, 298–304.

33 T. Yu, J. Liang, L. Luo, L. Wang, F. Zhao, G. Xu, X. Bai, R. Yang, S. Zhao, J. Wang, J. Yu and X. Sun, *Adv. Energy Mater.*, 2021, **11**, 2101915.

34 X. Ji, S. Hou, P. Wang, X. He, N. Piao, J. Chen, X. Fan and C. Wang, *Adv. Mater.*, 2020, **32**, 2002741.

35 H. Wan, B. Zhang, S. Liu, Z. Wang, J. Xu and C. Wang, *Adv. Energy Mater.*, 2024, **14**, 2303046.

36 W. E. Morgan, J. R. Van Wazer and W. J. Stec, *J. Am. Chem. Soc.*, 1973, **95**, 751–755.

37 S. Oswald, *Appl. Surf. Sci.*, 2015, **351**, 492–503.

38 Y. Sun, Y. Li, J. Sun, Y. Li, A. Pei and Y. Cui, *Energy Storage Mater.*, 2017, **6**, 119–124.

39 I. Takano, S. Isobe, T. A. Sasaki and Y. Baba, *Appl. Surf. Sci.*, 1989, **37**, 25–32.

40 S. Badrinarayanan, S. Sinha and A. B. Mandale, *J. Electron Spectrosc. Relat. Phenom.*, 1989, **49**, 303–309.

41 X. Ji, S. Hou, P. Wang, X. He, N. Piao, J. Chen, X. Fan and C. Wang, *Adv. Mater.*, 2020, **32**, 2002741.

42 H. Wan, B. Zhang, S. Liu, Z. Wang, J. Xu and C. Wang, *Adv. Energy Mater.*, 2023, **14**, 2303046.

43 Y.-C. Yin, J.-T. Yang, J.-D. Luo, G.-X. Lu, Z. Huang, J.-P. Wang, P. Li, F. Li, Y.-C. Wu, T. Tian, Y.-F. Meng, H.-S. Mo, Y.-H. Song, J.-N. Yang, L.-Z. Feng, T. Ma, W. Wen, K. Gong, L.-J. Wang, H.-X. Ju, Y. Xiao, Z. Li, X. Tao and H.-B. Yao, *Nature*, 2023, **616**, 77–83.